Journal of Materials Chemistry A

PAPER

View Article Online
View Journal | View Issue

Cite this: J. Mater. Chem. A, 2014, 2, 8223

An ultrasound-assisted deposition of NiO nanoparticles on TiO_2 nanotube arrays for enhanced photocatalytic activity

Zhi Wu,[a] Yingying Wang,[a] Lan Sun,*[ab] Yuxiao Mao,[a] Mengye Wang[a] and Changjian Lin[a]

Received 18th February 2014
Accepted 15th March 2014

DOI: 10.1039/c4ta00850b

www.rsc.org/MaterialsA

An ultrasound-assisted deposition technique was adopted to construct NiO nanoparticles on TiO_2 nanotube arrays (NiO–TiO_2 NTAs) which were prepared by three-step electrochemical anodization in an ethylene glycol system. The NiO nanoparticles were found to deposit on the surface of the highly oriented TiO_2 nanotubes. NiO–TiO_2 NTAs exhibited improved photochemical capability under UV irradiation. Compared with TiO_2 NTAs, a more than 2.56-fold enhancement in photocurrent response was achieved using the NiO–TiO_2 NTAs. The maximum incident photon to charge carrier generation efficiency (IPCE) values of NiO–TiO_2 NTAs and TiO_2 NTAs were 83.5% and 22.2%, respectively. The photocatalytic activities of NiO–TiO_2 NTAs were evaluated by the photodegradation of methylene blue (MB) aqueous solution. The kinetic constant of photocatalytic degradation of MB using NiO–TiO_2 NTAs prepared by ultrasonic deposition for 1.0 h was 1.9 times higher than that using TiO_2 NTAs. The enhanced photocurrent response and photocatalytic activity with NiO–TiO_2 NTAs were attributed to the formation of the NiO–TiO_2 p–n junctions.

1. Introduction

Nanostructured titanium dioxide (TiO_2), as a novel inorganic semiconductor material, has promising prospects in photocatalytic degradation of organic pollutants,[1,2] dye-sensitized solar cells,[3–5] hydrogen production by splitting water,[6,7] biological materials[8–10] and gas sensors[11,12] due to its exceptional properties such as high efficiency, chemical inertness, photostability, and low cost. However, these applications are mainly based on TiO_2 nanoparticles and nanotubes.[13,14] The disordered nanostructures and vast grain boundaries of TiO_2 nanoparticles lead directly to the small surface area and the fast recombination of photogenerated electron–hole pairs, which reduces the corresponding quantum efficiency. Compared to TiO_2 nanoparticles, the self-organized highly ordered TiO_2 nanotube arrays (TiO_2 NTAs) formed on the surface of the Ti substrate by electrochemical anodization have excellent photocatalytic activity and photoelectric conversion characteristics due to their unique architecture, large specific surface area, oriented charge transfer channel, contracted transport path, and thus a lower recombination rate of photogenerated charges.[15–17] It is widely accepted that the geometry and alignment of the nanotubes can greatly affect the performance of the nanotubes. To further enhance the photocatalytic activity of TiO_2 NTAs, the extremely highly ordered nanotubular TiO_2 arrays are desired. It has been demonstrated that the TiO_2 NTAs constructed through multi-anodization show appreciably more regular architecture than the TiO_2 NTAs fabricated by conventional single anodization under the same conditions.[18,19] During the three-step anodization, the well ordered hexagonal concaves distributed uniformly on the Ti substrate by the first anodization can serve as a template for further growth of TiO_2 nanotubes.[20] As a result, highly ordered TiO_2 NTAs with prominent nanostructure can be obtained. However, the photogenerated electron–hole pairs of TiO_2 are prone to recombine, which greatly limits the widespread application of TiO_2 in some of these fields.[21,22]

In recent years, several attempts have been made to enhance photocatalytic activity of TiO_2 nanostructured photocatalysis by suppressing recombination of photogenerated electron–hole pairs and improving the transport of photocarriers during photocatalysis.[7,21,23] Coupling semiconductors with appropriate band positions to improve the photocatalytic activity of TiO_2, such as CdSe[24] and $SrTiO_3$,[22,25] is an established issue because it can facilitate charge separation and enhance interfacial charge-transfer efficiency. Especially, the construction of a p–n junction is believed to be one of the most effective strategies due to the existence of an internal electric field in the interface.[26–28]

Nickel oxide (NiO), as a p-type transition element semiconductor, has received increasing attention in recent years.[14,29] It has an indirect band gap of about 3.55 eV,[30] and its

[a]State Key Laboratory of Physical Chemistry of Solid Surfaces, Department of Chemistry, College of Chemistry and Chemical Engineering, Xiamen University, Xiamen, 361005, China. E-mail: sunlan@xmu.edu.cn

[b]State Key Laboratory of Fine Chemicals, Dalian University of Technology, Dalian, 116024, China

conduction band lies above that of TiO_2. Since TiO_2 is a well-known n-type semiconductor, coupling TiO_2 with NiO seems to be a promising approach to enhance the photocatalytic efficiency, for the induced internal electric field, which resulted from the formation of p–n junctions, can markedly facilitate the separation of electron and hole.[13,31] Recently, NiO–TiO_2 composite nanotube arrays have been synthesized respectively by an electrochemical method[32] and an electroless plating method.[33] These methods were relatively simple but exhibited low control over the particle size and dispersion.

Herein, we present an ultrasound-assisted deposition technique to deposit NiO nanoparticles on the highly ordered TiO_2 NTAs with prominent nanostructure which were fabricated by a three-step electrochemical anodization approach in ethylene glycol with an appropriate amount of H_2O and NH_4F. The photoelectrochemical performance of NiO–TiO_2 NTAs was scrutinized. The photocatalytic activity of NiO–TiO_2 NTAs was evaluated by the photocatalytic degradation of methylene blue (MB) aqueous solution.

2. Experimental section

2.1 Preparation of three-step anodized TiO_2 NTAs

An electrochemical anodization of the Ti foils (2×1 cm^2) was carried out at room temperature in a conventional two-electrode cell with Pt as the counter electrode in ethylene glycol containing 0.3 wt% NH_4F + 2 vol% H_2O. In the first-step anodization, the 50 V potential was applied for 5 h for the growth of nanotubes. The as-anodized Ti foil was then ultrasonically rinsed with acetone to strip the anodized TiO_2 nanotubular layer from the Ti substrate, followed by rinsing with distilled water. Subsequently, the second-step anodization was conducted on the above Ti substrate at 50 V for 3 h. After ultrasonic removal of the TiO_2 layer again, the third step anodization was conducted on the exposed Ti foil at 50 V for 5 min. After three-step electrochemical anodization, the samples were rinsed with distilled water and dried in air. The as-prepared amorphous TiO_2 nanotube arrays were annealed in air at 350 °C for 2 h with a heating rate and cooling rate of 5 °C min^{-1} to convert to crystalline phases.

2.2 Preparation of NiO–TiO_2 NTAs

NiO nanoparticles were deposited on the three-step electrochemical anodized TiO_2 NTAs by ultrasound-assisted deposition. In a typical synthesis, the as-prepared TiO_2 NTAs were immersed in 0.2 M $NiCl_2$ ethanol solution and 0.2 M $NH_3 \cdot H_2O$ ethanol solution in turn and irradiated using an ultrasonic generator (KQ2200DB, Kunshan Ultrasonic Instrument Co., Ltd) with a frequency of 40 kHz and an ultrasonic intensity of 2.4 kW m^{-2} for the same desired time. Between each deposition step, the samples were rinsed with ethanol adequately to remove excess ions in the nanotube arrays. After ultrasonic deposition in both 0.2 M $NiCl_2$ ethanol solution and 0.2 M $NH_3 \cdot H_2O$ ethanol solution for 0.5 h, 1.0 h and 1.5 h respectively, the samples were rinsed with distilled water and dried in air and then annealed in air at 550 °C for 1 h with a heating rate and cooling rate of 5 °C min^{-1}.

2.3 Characterization of NiO–TiO_2 NTAs

The structure and morphology of NiO–TiO_2 NTAs were examined using a field emission scanning electron microscope (SEM, Hitachi-S4800). The crystalline phase of the prepared NiO–TiO_2 NTAs was identified by X-ray diffraction (XRD, Philips, PANalytical X'pert, Cu Kα radiation ($\lambda = 1.5417$ Å)). X-ray photoelectron spectroscopy (XPS, VG, Physical Electrons Quantum 2000 Scanning Esca Microprob, Al-Kα X-ray (1486.6 eV) at 15 kV and 35 W radiation) was employed to analyze the chemical composition and the concentration of atoms of the NiO–TiO_2 NTAs. The binding energies were normalized to the signal for adventitious C 1s at 284.8 eV. UV-vis diffuse reflection spectra (DRS) were recorded in the range of 200–600 nm at room temperature using a Varian Cary-5000 spectrophotometer. Photoluminescence (PL) measurements were carried out at room temperature by using a fluorescence spectrophotometer (Hitachi F-7000) with a xenon lamp as the excitation source ($\lambda_{ex} = 360$ nm).

2.4 Photoelectrochemical measurements

The photoelectrochemical measurements were carried out by using a 263 A potentiostat/galvanostat with an M5210 lock-in amplifier/chopper setup (using a chopper frequency of 34 Hz) connected to an SBP 300 grating spectrometer with an LHX 150 W Xe lamp as the source of illumination. The wavelength-dependent spectral response was measured in 0.5 M KOH aqueous solution at zero bias (VS SCE) in the range of 300–450 nm in a standard three electrode configuration with the as-synthesized samples (2×1 cm^2) as the working electrode, a saturated calomel electrode (SCE) and a platinum wire served as the reference electrode and the counter electrode, respectively.

2.5 Photocatalytic measurements

The photocatalytic (PC) activities of the prepared NiO–TiO_2 NTAs were investigated by using MB aqueous solution with an initial concentration of 10 mg L^{-1} as model pollutant. A 200 W high-pressure mercury lamp was employed as the simulated ultraviolet source. The distance between the samples and the lamp was 10 cm. Prior to photocatalytic degradation, the samples were soaked in 30 mL MB aqueous solution with continuous stirring at 30 °C in a thermostatic water cycle system while bubbling with air for 30 min to establish adsorption equilibrium. The concentration of MB was analyzed every 30 min by using a UV-vis spectrophotometer (Unico UV-2102PC, U.S.) at a wavelength of 664 nm.

3. Results and discussion

Fig. 1a shows the top-view SEM image of TiO_2 NTAs. The TiO_2 NTAs prepared through three-step electrochemical anodization exhibited a great orderliness with an average tube diameter of about 90 nm and a wall thickness of about 50 nm. The well-aligned highly ordered one-dimensional architecture with

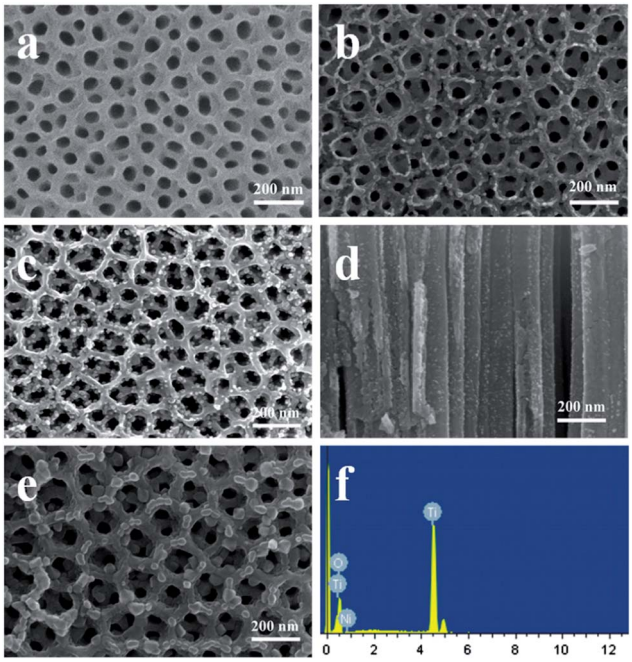

Fig. 1 SEM images of TiO_2 NTAs (a) and NiO–TiO_2 NTAs after ultrasound-assisted deposition for 0.5 h (b), 1.0 h (c and d) and 1.5 h (e) and (f) the EDX spectrum of NiO–TiO_2 NTAs after ultrasound-assisted deposition for 1.5 h.

smooth top surfaces was tight in arrangement with a double-layer of the nanoporous structure, which is highly favourable for uniform deposition of NiO nanoparticles. Fig. 1b–e show the SEM images of TiO_2 NTAs after ultrasonic deposition in 0.2 M $NiCl_2$ ethanol solution and 0.2 M $NH_3 \cdot H_2O$ ethanol solution in turn for 0.5, 1.0 and 1.5 h, respectively. A small amount of NiO nanoparticles were deposited on the surface of TiO_2 NTAs and were dispersed mainly around the nanotube entrance for the sample with 0.5 h deposition (Fig. 1b). When the deposition time was prolonged to 1.0 h, the amount of NiO nanoparticles on nanotubes markedly increased, and the NiO nanoparticles with an average size of about 8 nm were uniformly deposited on the top of TiO_2 nanotubes (Fig. 1c). The corresponding cross-sectional SEM image (Fig. 1d) shows that a lot of NiO nanoparticles were deposited inside the TiO_2 nanotubes. When the deposition time was increased to 1.5 h, the nanoparticle size increased significantly to 45 nm, and some of them even clogged at the nanotube entrance (Fig. 1e). Obviously, the highly ordered tubular structure of TiO_2 NTAs was not damaged by ultrasonic deposition. The composition of the samples was determined by EDX spectroscopy. It is observed from Fig. 1f that the as-prepared NiO–TiO_2 NTA sample prepared by ultrasonic deposition for 1.5 h contains Ti, O, and Ni, and the atomic percentage of Ni is 0.78%.

The nanoparticles deposited on/inside TiO_2 nanotubes were determine by TEM. Fig. 2a is a TEM image of the as-synthesized NiO–TiO_2 NTA sample. The ordered TiO_2 nanotubes are filled with the nanoparticles. Fig. 2b presents a high magnification TEM image of the area marked in Fig. 2a. The fringe spacing of 0.360 nm corresponds to the (101) crystallographic plane of

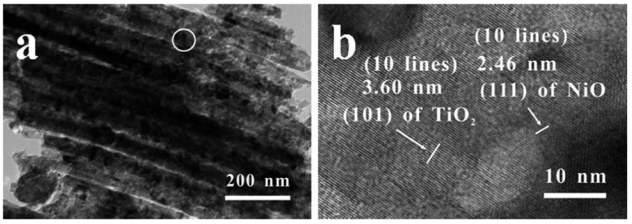

Fig. 2 (a) TEM image of NiO–TiO_2 NTAs and (b) HRTEM image of the area marked in (a).

anatase TiO_2 and the lattice spacing of approximate 0.246 nm matches the interplanar spacing of the (111) plane of NiO.

Fig. 3 shows the XRD patterns of the TiO_2 NTAs before and after the deposition of NiO nanoparticles. The TiO_2 NTAs consisted of the anatase phase ($2\theta = 25.3^\circ$, JCPDS no. 21-1272). After NiO deposition, all diffraction peaks can be assigned to the 100% anatase TiO_2 and Ti substrate, implying that there has been virtually no phase change in TiO_2 after the loading of NiO. However, no discernible peaks associated with crystalline phases of NiO were observed in the patterns of NiO–TiO_2 NTAs. The possible reason is that only a limited amount of NiO particles were loaded on TiO_2 NTAs so that the amount of NiO was below the XRD detection limit.

The chemical composition of NiO–TiO_2 NTAs was analyzed by XPS. Fig. 4a shows the XPS survey spectrum of NiO–TiO_2 NTAs. The sharp photoelectron peaks appeared at binding energies of 853.6 (Ni 2p), 532.0 (O 1s), 460.0 (Ti 2p), and 285.6 eV (C 1s), indicating that the sample contained Ti, O, Ni, and C elements. The C peak was ascribed to adventitious hydrocarbon from the XPS instrument itself. The higher resolution XPS spectrum of the Ni 2p region is displayed in Fig. 4b. Peak fitting to the spectra was applied using a Gaussian–Lorentzian peak shape after subtraction of Shirley background. The Ni 2p XPS spectra were fitted into four peaks at 855.86, 861.95, 873.39 and 880.93 eV. The peaks located at approximately 855.86 and 861.95 eV can be assigned to the binding energies of Ni $2p_{3/2}$ and the peaks at 873.39 and 880.93 eV can be attributed to Ni $2p_{1/2}$, indicating the existence of NiO.[34,35] Fig. 4c shows the high-resolution XPS spectrum of O 1s. The oxygen on the sample

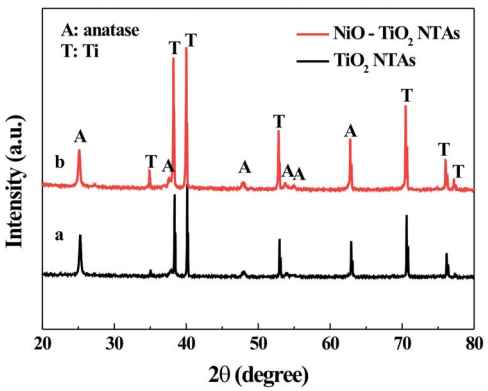

Fig. 3 XRD spectra of TiO_2 NTAs and NiO–TiO_2 NTAs.

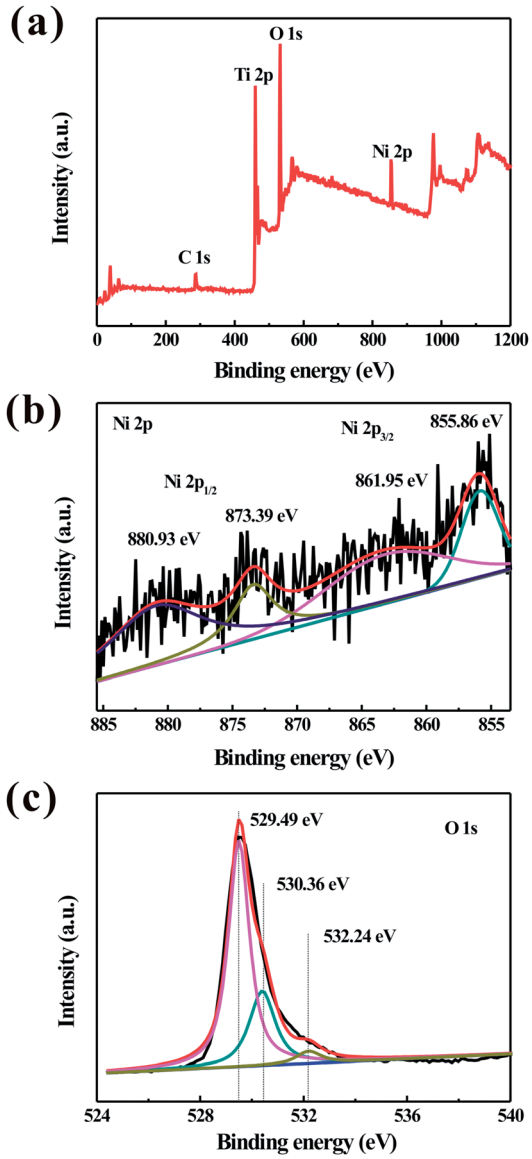

Fig. 4 Survey XPS spectrum of NiO–TiO_2 NTAs (a) and high resolution XPS spectra of Ni 2p (b) and O 1s (c) of NiO–TiO_2 NTAs.

surface existed in the form of the binding energies of 532.24, 530.36 and 529.49 eV. The main peak at 529.49 eV could be ascribed to the O lattice of TiO_2 and the binding energy of 530.36 eV can be associated with O in NiO nanoparticles.[35,36] The peak at 532.24 eV is attributed to irreversibly adsorbed water molecules on the surface of the NiO/TiO_2 sample.[14]

Fig. 5 shows the absorption spectra of the NiO–TiO_2 NTAs with different ultrasonic times. The absorption onset of TiO_2 NTAs was at about 390 nm, which is consistent with the intrinsic bandgap absorption of anatase TiO_2 (~3.2 eV). In addition, two characteristic absorption peaks of TiO_2 at about 410 nm and 540 nm corresponded to the absorption of the trapped hole and the trapped electron, respectively, which result from the sub-bandgap of surface defects on TiO_2 nanotubes.[37] Compared with the pure TiO_2 NTAs, NiO–TiO_2 NTAs exhibit an increased absorption in the UV light region and the

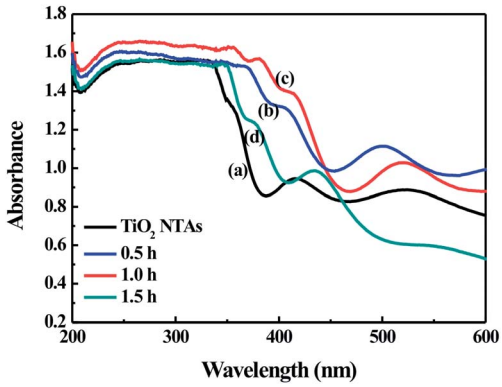

Fig. 5 UV-vis diffuse reflectance spectra of TiO_2 NTAs and NiO–TiO_2 NTAs prepared under different ultrasonic times.

band edges of the samples were shifted toward the visible-light region (red shift). It has been reported that the Ni d orbit may be essential to decrease the energy gap between Ti (d) and O (p) orbitals of Ti oxide to enable the red-shift absorption.[33,38] It is widely accepted that the higher light absorption under the same conditions indicates the better photocatalytic activity of the photocatalysis.[39] The NiO–TiO_2 NTAs after ultrasonic deposition for 1.0 h possessed the strongest absorption among all samples, and thus the highest photocatalytic activity was expected.

Fig. 6a shows the photocurrent spectra of the as-prepared samples in 0.5 M KOH aqueous solution. The maximum value

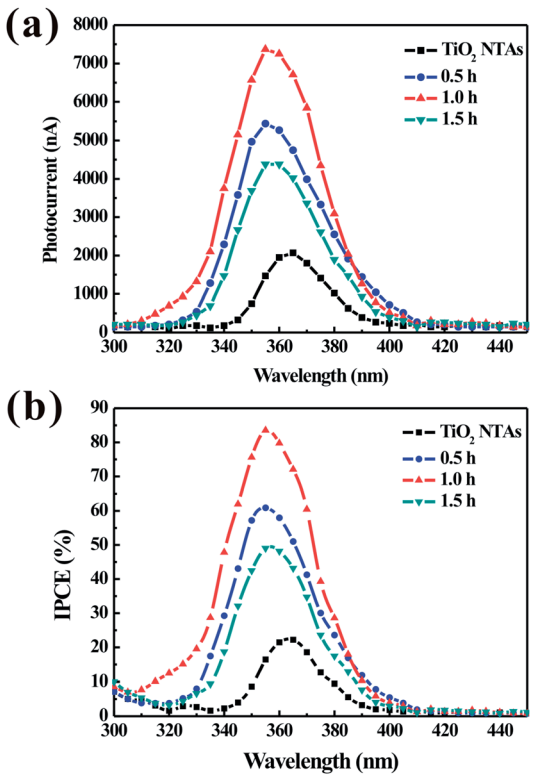

Fig. 6 (a) The wavelength-dependent spectral response and (b) the photo-conversion efficiency of TiO_2 NTAs and NiO–TiO_2 NTAs prepared under different ultrasonic times.

(~7369 nA) was obtained at 355 nm by the NiO–TiO_2 NTAs after ultrasonic deposition for 1.0 h, which is 3.56 times that of pure TiO_2 NTAs (2070 nA). The photocurrent of NiO–TiO_2 NTAs prepared by ultrasonic deposition for 0.5 h is low due to the small amount of NiO nanoparticles while the photocurrent of NiO–TiO_2 NTAs prepared by the ultrasonic deposition for 1.5 h decreased sharply because of the big nanoparticle size.[40] The incident photon to charge carrier generation efficiency (IPCE) at different wavelengths is determined from the short circuit photocurrents (I_{sc}) monitored at different excitation wavelengths (λ) to compare the photoresponse of the samples using an equation[41]

$$\text{IPCE (\%)} = [1240 \times I_{sc}\ (\text{A cm}^{-2})]/\lambda\ (\text{nm}) \times I_{inc}\ (\text{W cm}^{-2})] \times 100 \quad (1)$$

where I_{inc} is the incident light power. The IPCE as a function of the excitation wavelength for TiO_2 NTAs and NiO–TiO_2 NTAs calculated from the data of Fig. 6a is shown in Fig. 6b. A maximum IPCE of 83.5% was achieved for the NiO–TiO_2 NTA electrode prepared by ultrasonic deposition for 1.0 h at a wavelength of 335 nm. However, under the same conditions, the IPCE values of 22.2% was achieved for the TiO_2 NTA electrode. Lower IPCE values indicate that a larger fraction of carriers is lost to charge recombination.

The efficiency of charge carrier trapping, immigration and transfer was investigated by the photoluminescence emission spectra. In general, the photoluminescence of nanostructure materials is related to self-trapping excitation, oxygen vacancy, and its surface states.[42] Fig. 7 is PL spectra of TiO_2 NTAs and NiO–TiO_2 NTAs. The peaks at about 452 nm, 469 nm, 486 nm, and 595 nm were ascribed to shallow trap levels resulting from oxygen vacancy of TiO_2 NTAs.[43,44] The lower the photoluminescence intensity indicates the higher separation and transfer efficiency of photogenerated electron–hole pairs and thus a higher photocatalytic quantum yield.[45] The photoluminescence intensity decreases in the order of 1.0 h-NiO–TiO_2 NTAs < 0.5 h-NiO–TiO_2 NTAs < 1.5 h-NiO–TiO_2 NTAs < TiO_2 NTAs. This implies that the presence of NiO nanoparticles reduces the possibility of the electron–hole recombination, especially for the NiO–TiO_2 NTAs prepared by ultrasonic deposition for 1.0 h.

To investigate the photo-induced applications of NiO–TiO_2 NTAs, the photocatalytic activity of the samples was evaluated by the degradation of methylene blue (MB) aqueous solution under UV irradiation. The degradation reactions for all samples obey pseudo-first-order reaction kinetics, which could be expressed by $\ln(C/C_0) = -kt$, where k, C_0 and C is the apparent first-order reaction constant, the initial and the reaction concentrations of MB, respectively. The time-evolved photodecomposition curves of the TiO_2 NTAs and NiO–TiO_2 NTAs are shown in Fig. 8a. During the selfdegradation, the concentration of MB was only reduced by 4.8% after 120 min irradiation. When using TiO_2 NTAs as the photocatalyst, the concentration of MB was reduced by 25.6%. It is noteworthy that the NiO–TiO_2 NTAs obtained by ultrasonic deposition for 0.5, 1.0 and 1.5 h displayed higher photocatalytic activities than TiO_2 NTAs, and the concentration of MB was reduced by 53.1%, 58.1% and 45.5%, respectively. Fig. 8b compares the MB degradation kinetic curves of TiO_2 NTAs and NiO–TiO_2 NTAs prepared under different ultrasonic times. The reaction constants k for TiO_2 NTAs and NiO–TiO_2 NTAs obtained by ultrasonic deposition for 0.5, 1.0 and 1.5 h were calculated to be 2.49×10^{-3}, 6.35×10^{-3}, 7.30×10^{-3} and 5.05×10^{-3} min^{-1}, respectively. It is apparent that the NiO–TiO_2 NTAs show an increased activity in comparison with the pure TiO_2 NTAs in the photocatalytic processes, and the kinetic constants of MB degradation with NiO–TiO_2 NTAs after ultrasonic deposition for 1.0 h acting as photocatalysis was 2.93 times of that of pure TiO_2 NTAs, proving that the NiO nanoparticles deposited on TiO_2 NTAs significantly enhanced the photocatalytic activity of TiO_2 NTAs.

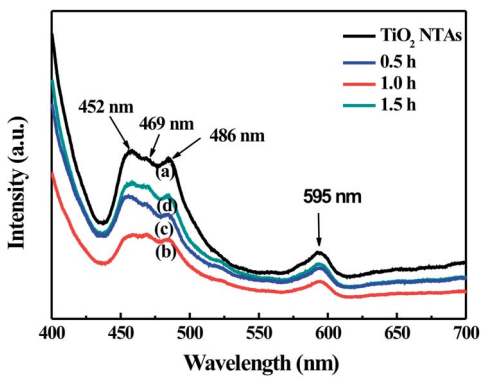

Fig. 7 PL spectra of TiO_2 NTAs and NiO–TiO_2 NTAs prepared under different ultrasonic times.

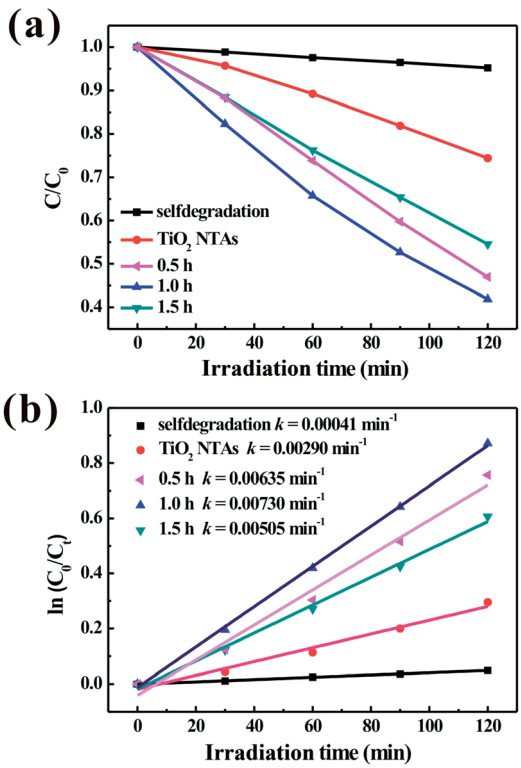

Fig. 8 Photodegradation rates of MB for TiO_2 NTAs and NiO–TiO_2 NTAs prepared under different ultrasonic times.

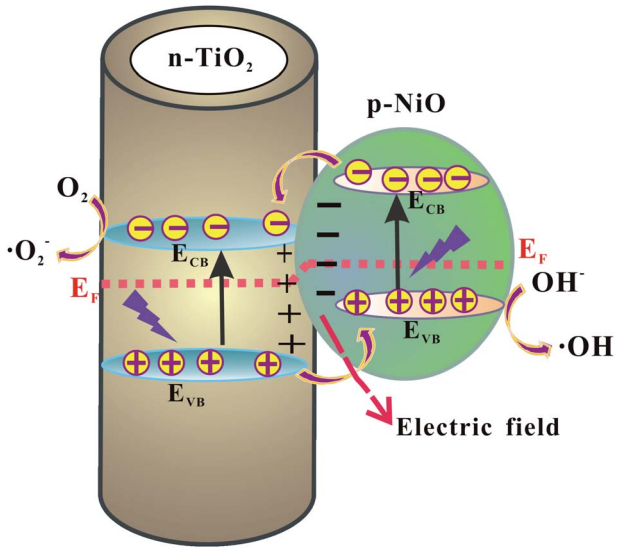

Fig. 9 Schematic diagram showing the separation and transfer of charge carriers in the p-type NiO/n-type TiO_2 heterojunction under UV irradiation.

The enhanced photocatalytic activity of NiO–TiO_2 NTAs is mainly attributed to the p–n junction effect between p-type NiO and n-type TiO_2 heterojunction. To understand how the p–n junctions work, the proposed schematic energy-level diagram of p-type NiO and n-type TiO_2 is illustrated in Fig. 9. The Fermi energy level of n-type TiO_2 lies closer to the conduction band while the Fermi energy level of p-type NiO lies closer to the valence band. A number of p–n junctions will be formed when NiO nanoparticles and TiO_2 nanotubes integrate, which will induce the inner electric field in the interface.[26] In this process, the electrons in the n-type TiO_2 flow into some of the holes in the p-type NiO because these holes are available at lower-energy states, and the energy band of NiO moves up while the energy band of TiO_2 moves down along with the diffusion of carriers until thermal equilibrium is established, forming a constant Fermi energy. At the equilibrium, the inner electric field makes the p-type semiconductor NiO region negatively charged, while the TiO_2 region has the positive charge.[14] Under UV irradiation, the photogenerated electron–hole pairs created on the n-type semiconductor TiO_2 surface drifted by the electric field in the opposite direction. The holes flow into the negative field and the electrons move to the positive field. Thus, the photogenerated holes at the valence band of TiO_2 will move towards the p-type NiO and the electrons towards the n-type TiO_2 under the effect of the inner electric field.[13] As a result, photogenerated electron–hole pairs are separated efficiently and the photocatalytic activity is enhanced.

4. Conclusion

In summary, we successfully synthesized NiO–TiO_2 NTAs through deposition of NiO nanoparticles on TiO_2 NTAs obtained by three-step electrochemical anodization using an ultrasound-assisted deposition. NiO nanoparticles were uniformly dispersed on and inside the TiO_2 nanotubes. NiO nanoparticles greatly promoted the separation and transfer of photogenerated charges and thus effectively enhanced the photo-conversion efficiency and photocatalytic activity of TiO_2 NTAs under UV irradiation. The ultrasound-assisted deposition technique described in this study provides a simple and facile approach to synthesize highly dispersed nanoparticle-modified one-dimensional nanomaterials.

Acknowledgements

This work was supported by the National Natural Science Foundation of China (21321062), the Natural Science Foundation of Fujian Province of China (2011J01057), the State Key Laboratory of Fine Chemicals (KF1104) and NFFTBS (J1310024).

Notes and references

1 J. M. Macak, M. Zlamal, J. Krysa and P. Schmuki, *Small*, 2007, **3**, 300–304.
2 H. Lachheb, E. Puzenat, A. Houas, M. Ksibi, E. Elaloui, C. Guillard and J.-M. Herrmann, *Appl. Catal., B*, 2002, **39**, 75–90.
3 G. K. Mor, K. Shankar, M. Paulose, O. K. Varghese and C. A. Grimes, *Nano Lett.*, 2006, **6**, 215–218.
4 J. Wang and Z. Lin, *Chem. – Asian J.*, 2012, **7**, 2754–2762.
5 X. Xin, J. Wang, W. Han, M. Ye and Z. Lin, *Nanoscale*, 2012, **4**, 964–969.
6 G. K. Mor, K. Shankar, M. Paulose, O. K. Varghese and C. A. Grimes, *Nano Lett.*, 2005, **5**, 191–195.
7 M. Ye, J. Gong, Y. Lai, C. Lin and Z. Lin, *J. Am. Chem. Soc.*, 2012, **134**, 15720–15723.
8 L. Peng, A. D. Mendelsohn, T. J. LaTempa, S. Yoriya, C. A. Grimes and T. A. Desai, *Nano Lett.*, 2009, **9**, 1932–1936.
9 Y. Lai, L. Lin, F. Pan, J. Huang, R. Song, Y. Huang, C. Lin, H. Fuchs and L. Chi, *Small*, 2013, **9**, 2945–2953.
10 Y. Lai, F. Pan, C. Xu, H. Fuchs and L. Chi, *Adv. Mater.*, 2013, **25**, 1682–1686.
11 Q. Zheng, B. Zhou, J. Bai, L. Li, Z. Jin, J. Zhang, J. Li, Y. Liu, W. Cai and X. Zhu, *Adv. Mater.*, 2008, **20**, 1044–1049.
12 G. K. Mor, O. K. Varghese, M. Paulose, K. G. Ong and C. A. Grimes, *Thin Solid Films*, 2006, **496**, 42–48.
13 C. Shifu, Z. Sujuan, L. Wei and Z. Wei, *J. Hazard. Mater.*, 2008, **155**, 320–326.
14 J. Yu, W. Wang and B. Cheng, *Chem. – Asian J.*, 2010, **5**, 2499–2506.
15 Z. Liu, X. Zhang, S. Nishimoto, M. Jin, D. A. Tryk, T. Murakami and A. Fujishima, *J. Phys. Chem. C*, 2008, **112**, 253–259.
16 Z. Liu, X. Zhang, S. Nishimoto, T. Murakami and A. Fujishima, *Environ. Sci. Technol.*, 2008, **42**, 8547–8551.
17 Q. Zhao, X. Li, N. Wang, Y. Hou, X. Quan and G. Chen, *J. Nanopart. Res.*, 2009, **11**, 2153–2162.
18 Y. Shin and S. Lee, *Nano Lett.*, 2008, **8**, 3171–3173.
19 J. Gong, Y. Lai and C. Lin, *Electrochim. Acta*, 2010, **55**, 4776–4782.

20 G. Zhang, H. Huang, Y. Zhang, H. Chan and L. Zhou, *Electrochem. Commun.*, 2007, **9**, 2854–2858.
21 H. Y. Yang, S. F. Yu, S. P. Lau, X. Zhang, D. D. Sun and G. Jun, *Small*, 2009, **5**, 2260–2264.
22 J. Ng, S. Xu, X. Zhang, H. Y. Yang and D. D. Sun, *Adv. Funct. Mater.*, 2010, **20**, 4287–4294.
23 X. Xin, H. Y. Liu, M. Ye and Z. Lin, *Nanoscale*, 2013, **5**, 11220–11226.
24 C. Harris and P. V. Kamat, *ACS Nano*, 2009, **3**, 682–690.
25 J. Zhang, J. H. Bang, C. Tang and P. V. Kamat, *ACS Nano*, 2009, **4**, 387–395.
26 Z. Zhang, C. Shao, X. Li, C. Wang, M. Zhang and Y. Liu, *ACS Appl. Mater. Interfaces*, 2010, **2**, 2915–2923.
27 H. He, P. Xiao, M. Zhou, Y. Zhang, Q. Lou and X. Dong, *Int. J. Hydrogen Energy*, 2012, **37**, 4967–4973.
28 M. Wang, L. Sun, Z. Lin, J. Cai, K. Xie and C. Lin, *Energy Environ. Sci.*, 2013, **6**, 1211–1220.
29 A. Hakim, J. Hossain and K. A. Khan, *Renewable Energy*, 2009, **34**, 2625–2629.
30 G. Boschloo and A. Hagfeldt, *J. Phys. Chem. B*, 2001, **105**, 3039–3044.
31 S. Liu, T. Xie, Z. Chen and J. Wu, *Appl. Surf. Sci.*, 2009, **255**, 8587–8592.
32 L. L. Wang, S. C. Zhang and X. M. Wu, *Chem. Lett.*, 2011, **40**, 1428–1430.
33 J. Guo, W. Fu, H. Yang, Q. Yu, W. Zhao, X. Zhou, Y. Sui, J. Ding, Y. Li, S. Cheng and M. Li, *J. Phys. D: Appl. Phys.*, 2010, **43**, 245202.
34 V. Biju, *Mater. Res. Bull.*, 2007, **42**, 791–796.
35 B. Sasi and K. Gopchandran, *Nanotechnology*, 2007, **18**, 115613.
36 L. C. Sim, K. W. Ng, S. Ibrahim and P. Saravanan, *Int. J. Photoenergy*, 2013, **2013**, 1–10.
37 Y. Lai, L. Sun, Y. Chen, H. Zhuang, C. Lin and J. W. Chin, *J. Electrochem. Soc.*, 2006, **153**, D123.
38 G. K. Mor, H. E. Prakasam, O. K. Varghese, K. Shankar and C. A. Grimes, *Nano Lett.*, 2007, **7**, 2356–2364.
39 C. Lettmann, K. Hildenbrand, H. Kisch, W. Macyk and W. F. Maier, *Appl. Catal., B*, 2001, **32**, 215–227.
40 Y. Zhang, X. Li, X. Hua, N. Ma, D. Chen and H. Wang, *Scr. Mater.*, 2009, **61**, 296–299.
41 I. Robel, V. Subramanian, M. Kuno and P. V. Kamat, *J. Am. Chem. Soc.*, 2006, **128**, 2385–2393.
42 L. Forss and M. Schubnell, *Appl. Phys. B*, 1993, **56**, 363–366.
43 N. Serpone, D. Lawless and R. Khairutdinov, *J. Phys. Chem.*, 1995, **99**, 16646–16654.
44 P. M. Kumar, S. Badrinarayanan and M. Sastry, *Thin Solid Films*, 2000, **358**, 122–130.
45 L. Jing, Y. Qu, B. Wang, S. Li, B. Jiang, L. Yang, W. Fu, H. Fu and J. Sun, *Sol. Energy Mater. Sol. Cells*, 2006, **90**, 1773–1787.